



# Magnetic mining waste based-geopolymers applied to catalytic reactions with ozone

Daniela Gier Della Rocca<sup>a,\*</sup>, Flávio Augusto Santos e Sousa<sup>a</sup>,  
José Domingos Ardisson<sup>b</sup>, Rosely Aparecida Peralta<sup>c</sup>, Enrique Rodríguez-Castellón<sup>d</sup>,  
Regina de Fátima Peralta Muniz Moreira<sup>a</sup>

<sup>a</sup> Laboratory of Energy and Environment (LEMA), Department of Chemical and Food Engineering, Federal University of Santa Catarina (UFSC), 88040-900 Florianópolis, SC, Brazil

<sup>b</sup> Laboratory of Applied Physics, Center for the Development of Nuclear Technology, Federal University of Minas Gerais, 30123-970, Belo Horizonte, MG, Brazil

<sup>c</sup> Laboratory of Bioinorganic and Crystallography Laboratory (LABINC), Department of Chemistry, Federal University of Santa Catarina (UFSC), 88040-900 Florianópolis, SC, Brazil

<sup>d</sup> Department of Inorganic Chemistry, Science Faculty, University of Málaga, 29010, Málaga, Spain

## ARTICLE INFO

### Keywords:

Alkali-activated aluminosilicates  
Iron oxides  
Advanced oxidation processes  
Mining waste  
Heterogeneous catalysis

## ABSTRACT

The demand for sustainable and low-cost materials for wastewater treatment is increasing considerably. In this scenario, geopolymers have gained great interest, due to their good mechanical properties, their ability to be produced from industrial waste and their adsorbent or catalytic properties. In this study, novel magnetic mining waste based-geopolymers were produced by incorporating a residue from phosphate waste rocks, which were extensively characterized (XRD, TGA/DTA, SEM, BET, XRF, FTIR, Mössbauer, ss-NMR and XPS). The materials produced showed formation of a dense framework, even with 75% incorporation of the residue. The iron oxides and their magnetic properties remained unchanged, and their application in advanced oxidation reactions were evaluated, in particular, as catalysts in ozonation reactions. All of the geopolymers presented catalytic activity in the ozonation reaction, with catalytic ozone decomposition values of up to  $2.98 \text{ min}^{-1}$ , which is 99 times greater than non-catalyzed reactions. Moreover, the reuse (performed in three cycles) and hot filtration-like experiments demonstrated, respectively, the regenerability and heterogeneous catalytic properties of the produced materials, showcasing the potential of these waste materials for catalytic geopolymer production. demonstrating the potential of this waste to produce catalytic geopolymers.

## 1. Introduction

Geopolymers (GPs) have been studied recently as environmentally-friendly and low-cost materials [1,2], due to their special properties and application in different areas. GPs are inorganic polymers formed from aluminosilicates in the presence of an alkaline activator [3], and many different applications have been proposed, as in: cement, ceramics, fire-proof materials, as drug support, adsorbents, membrane filters and catalyst/catalyst support, among others [4–9].

\* Corresponding author.

E-mail address: [danigierdellarocca@gmail.com](mailto:danigierdellarocca@gmail.com) (D. Gier Della Rocca).

<https://doi.org/10.1016/j.heliyon.2023.e17097>

Received 22 February 2023; Received in revised form 31 May 2023; Accepted 7 June 2023

Available online 8 June 2023

2405-8440/© 2023 The Authors. Published by Elsevier Ltd. This is an open access article under the CC BY-NC-ND license (<http://creativecommons.org/licenses/by-nc-nd/4.0/>).

Despite these many uses, conventional geopolymers do not usually show good performance in wastewater treatment. Thus, the addition of different catalysts and additives are required to enable this material to be efficient for pollutant removal [10–12]. Catalytic geopolymers (CGPs) have removed high levels of pollutants dissolved in water (~100%) [13–15] and have low manufacturing costs than most currently used catalysts (up to 72% lower) [16,17] and their activity makes them suitable for testing in advanced oxidation processes (AOP) [18]. CGPs have mainly been used in photocatalytic oxidation and their application in other AOPs, such as catalytic ozonation, is scarcely investigated.

Geopolymers and zeolites have similar chemical composition, but different characteristics related to their crystallinity and textural properties. While catalytic ozonation using zeolite is well studied, the use of geopolymers in these reactions is not well documented [1, 5]. Ozone itself ( $O_3$ ) has a high oxidizing potential ( $E^\circ = 2.08$  V) [19], rapidly reacting with electron-rich groups, double or triple bonds and activated aromatic rings [20]. The non-catalytic reactions in aqueous phase mainly occur at basic pH (>8), since  $O_3$  interacts with  $OH^-$  anions, leading to the formation of  $\bullet OH$ , which is even more oxidizing [21,22]. However, at acidic pH values, the lack of  $OH^-$  drastically reduces the generation rate of reactive oxidizing species, and requires the addition of a catalyst to improve the catalytic performance process.

Iron-based catalysts [23,24] and zeolites [25] are known to be highly active in catalytic ozonation reactions, enabling the application of ozonation in aqueous suspensions under acidic conditions. For instance, magnetite has strong catalytic behavior in oxidizing organic pollutants in water and can be easily removed using magnetic separation [24,26]. In many cases, magnetite and other iron oxide species are segregated by applying a magnetic field and then disposed as industrial residue. More especially, in mining activity, this waste represents approximately 15% of the ore mass [27], causing substantial environmental problems and high costs for its suitable disposal [20].

In this study, we prepared geopolymers using magnetic waste from phosphate mining, which could be applied to catalytic ozonation processes in aqueous suspension. Different formulations were investigated, characterized and their kinetics of ozone decomposition in the aqueous suspension was studied under acidic conditions.

## 2. Methodology

### 2.1. Chemicals and materials

Kaolin was obtained from the company Caulisa (Campina Grande, PB, Brazil) and transformed into metakaolin (MK) through calcination in a muffle furnace (Fornitec brand, model F2-DM) at 900 °C for 1 h, with a heating rate of 5 °C·min<sup>-1</sup>. Magnetic mining waste (MMW) from phosphate mining was supplied by a Brazilian company. The MMW was dried in an oven at 110 °C for 12 h. Then the residue was sieved through a 200-mesh sieve at room temperature and the fine material obtained was used to produce the geopolymers. Sodium silicate ( $SiO_2:Na_2O$ , 3:2 M ratio) was purchased from Quimidrol (Brazil). Sodium hydroxide (NaOH, 98% purity) and monosodium hydrogen phosphate ( $NaH_2PO_4$ , 99% purity) were obtained from Vetec (Brazil). Phosphoric acid ( $H_3PO_4$ , 85% purity) was acquired from Merck.

### 2.2. Geopolymer synthesis

Four different geopolymer formulations (Table 1) were prepared using MMW:MK mass ratios in the range of 0–8.33 and the same oxides molar ratio (Table S1), based on values already reported in the literature for appropriate mechanical properties [28]. The mass percentage of each precursor material was calculated considering its chemical composition (Table 1).

The GPs were synthesized as follows. Firstly, NaOH was dissolved in deionized water, and  $Na_2SiO_3$  was added to the mixture. Next, the solids MK and MMW (when applied) were slowly added. This mixture was stirred for 15 min until complete homogenization. The samples were then molded into acrylic cylinders ( $D = 27$  mm and  $H = 48$  mm) and cured for 2 days in an oven at 65 °C. In the next step, the GPs were demolded, submerged in deionized water and cured for an additional 26 days at room temperature. The submerged curing process removes the unreacted sodium ions from the solid surface and avoids interference from the  $CO_2$  adsorption process [29]. Lastly, the GPs produced were cracked into small particles, macerated, sieved through a 200-mesh sieve, and the fine particles obtained were stored for their analyses and catalyst usage.

**Table 1**  
Mass percentage of the materials used to produce different geopolymers.

Sample	Precursor materials (wt%)				Water (wt%)
	MMW	MK	$Na_2SiO_3$	NaOH	$H_2O$
G1	0	35	55	6	4
G2	25	26	37	5	7
G3	50	18	20	4	8
G4	75	9	3	3	10

### 2.3. Characterization

Chemical compositions were measured by X-ray fluorescence (Panalytical-AXIOS Max) according to Brazilian technical standard NBR 12667/2014 (similar to ISO 12677 norm [30]). XRD analysis was conducted on a Rigaku Miniflex600 diffractometer (CuK $\alpha$  radiation,  $\lambda = 1.5418 \text{ \AA}$ ), at a speed of  $3^\circ \cdot \text{s}^{-1}$  from  $10^\circ$  to  $90^\circ$ . XRD patterns were retrieved from Joint Committee on Powder Diffraction Standards (JCPDS) of International Center for Diffraction Data (ICDD). Fourier transform infrared (FTIR) spectra were taken by an Agilent Technologies infra-red spectrophotometer (model Cary 600 Series, from 400 to  $4000 \text{ cm}^{-1}$ ). TGA/DTA were performed on a thermogravimetric analyzer (model DTG60/60H, Shimadzu), under inert atmosphere ( $\text{N}_2$ , 99.996% purity) and the heating rate applied was  $10^\circ \text{C min}^{-1}$  ( $25\text{--}900^\circ \text{C}$ ). The morphology and dimensions of the particles were observed by SEM (HITACHI TM3030, 15 kV), coupled with EDS. The Brunauer-Emmett-Teller surface area ( $S_{\text{BET}}$ ) and pore size diameter distribution, calculated by the Barrett-Joyner-Halenda (BJH) method, were obtained by nitrogen ( $\text{N}_2$ ) adsorption-desorption experiments (Autosorb 1C analyzer, Quantachrome, USA).

$^{57}\text{Fe}$  Mössbauer spectra were obtained in a transmission mode using a  $^{57}\text{Co}/\text{Rh}$  source without application of an external magnetic field at room temperature. Spectral hyperfine parameters were calculated using the Normos least-squares-fit software package [31]. Isomer shifts were given relative to  $\alpha\text{-Fe}$  at room temperature. In the measurements, sample holders with absorbers with about  $10 \text{ mg}$  of  $\text{Fe}/\text{cm}^2$  were used.

XPS spectra were performed on a Physical Electronics PHI VersaProbe II spectrometer (Physical Electronics, Chanhassen, MN, USA) with monochromatic Al-K $\alpha$  radiation ( $100 \mu\text{m}$ ,  $100 \text{ W}$ ,  $20 \text{ kV}$ ,  $1486.6 \text{ eV}$ ), and a charge neutralizer. The spectrometer was calibrated with Au  $4f_{7/2}$ , Ag  $3d_{5/2}$  and Cu  $2p_{3/2}$  photoelectron lines at  $84.0$ ,  $368.2$  and  $932.7 \text{ eV}$ , respectively. High-resolution spectra were recorded at a take-off angle of  $45^\circ$  by a multi-channel hemispherical electron analyzer operating in the constant pass energy mode at  $29.35 \text{ eV}$ . Adventitious carbon (C 1s at  $284.8 \text{ eV}$ ) was used as a reference. A Shirley-type background was subtracted from the signals and the deconvolution curves were fitted using the Gaussian–Lorentzian model in Multipack version 9.6.0.15 software. Surface atomic concentration percentages of the constituent elements were determined considering the corresponding area sensitivity factor for the different measured spectral regions.

Solid-state NMR spectra were acquired using a Bruker Avance-III HD 600 NMR spectrometer equipped with a  $14.1 \text{ T}$  narrow bore magnet operating at Larmor frequencies of  $600.09 \text{ MHz}$  for  $^1\text{H}$ ,  $156.37 \text{ MHz}$  for  $^{27}\text{Al}$  and  $119.21 \text{ MHz}$  for  $^{29}\text{Si}$ . Powdered samples were packed into a  $2.5 \text{ mm}$   $\text{ZrO}_2$  rotor and rotated at a magic-angle-spinning (MAS) rate of  $15 \text{ kHz}$  in a  $2.5 \text{ mm}$  triple-resonance DVT probe.  $^{27}\text{Al}$  determination was conducted by proton decoupling (continuous wave sequence) applying a single pulse ( $\pi/18$ ) with an excitation pulse of  $1 \mu\text{s}$  and a  $5 \text{ s}$  relaxation delay to obtain  $1000$  scans. Similarly,  $^{29}\text{Si}$  analysis was also performed with proton decoupling (continuous wave sequence) by applying a single pulse ( $\pi/2$ ) with an excitation pulse of  $5 \mu\text{s}$ , and a  $60 \text{ s}$  relaxation delay to obtain  $10,800$  scans. The chemical shifts were referenced to an external solution of tetramethylsilane ( $\delta^{29}\text{Si} = 0 \text{ ppm}$ ) and  $1 \text{ M}$  of  $\text{Al}(\text{NO}_3)_3$  ( $\delta^{27}\text{Al} = 0 \text{ ppm}$ ), for  $^{29}\text{Si}$  and  $^{27}\text{Al}$ , respectively. Spectral smoothing, baseline subtraction and multipeak fitting were carried out using OriginPro 2018.

The magnetic properties of the samples were determined and calculated with a vibrating sample magnetometer (VSM) from the KLA company, model Microsense EV9 (room temperature,  $\pm 20 \text{ kOe}$ ).

### 2.4. Catalytic ozonation reactions

Catalytic ozone decomposition was conducted at  $25 \pm 1^\circ \text{C}$ , in a  $1.5 \text{ L}$  glass-jacketed reactor (height  $21 \text{ cm}$  and diameter  $8 \text{ cm}$ ) under continuous stirring ( $\sim 600 \text{ rpm}$ , Dist, model DI-03, Brazil). Firstly,  $1 \text{ L}$  of buffered pH 4 solution ( $\text{NaH}_2\text{PO}_4/\text{H}_3\text{PO}_4$ ,  $100 \text{ mM}$ ) was prepared. In the next step,  $100 \text{ mg}$  of the corresponding CGP sample were added to the vessel and the ozone generator (O3R Philozon – model ID5) was quickly switched on, continuously bubbling through a porous stone diffuser ( $0.063 \text{ m}^3 \text{ h}^{-1}$ ,  $0.4 \text{ bar}$ ). At regular time intervals,  $5 \text{ mL}$  aliquots were collected from the reactor, filtered and analyzed, and the aqueous ozone concentration (indigo colorimetric method, ISO 4500 [30]) was measured. All tests were conducted at least in duplicate.

The previously described process consists of one reaction cycle. At the end of the ozonation time, the suspension was filtered (PVDF membrane,  $0.22 \mu\text{m}$ ) to collect the solids. They were washed with deionized water ( $250 \text{ mL}$ ) to remove possible buffer reactants. Next, the geopolymer was dried (in  $40^\circ \text{C}$  oven for  $1 \text{ d}$ ). Then, the solids were applied to a new ozonation reaction with the same previous condition, i.e., a new cycle. The catalysts were submitted to three cycles each, to observe their catalytic effect.

Furthermore, a modified hot filtration methodology [32] was also applied to guarantee that heterogeneous, and not homogeneous, reactions occurred. Briefly, the first cycle aqueous filtrate was collected and stored for  $1 \text{ d}$  to allow all the dissolved ozone to leave the solution. Then,  $1 \text{ L}$  of the filtered buffer solution was added to the reactor and the experimental procedure was conducted as previously described, but without the addition of a catalyst. The aqueous ozone concentration was measured to compare it with the with the catalytic results. The aqueous filtrate was also submitted to atomic absorption spectroscopy (AAS) (Agilent 240 FSAA spectrophotometer) to determine if Si, Al or Fe leaching occurred, using the direct nitrous oxide-acetylene flame method for Si and Al and the direct air-acetylene flame method for Fe, as described in ISO 3111D and ISO 3111 B, respectively [30]. The minimum quantification limits (MQL) for Si, Al and Fe were, in this order:  $300 \mu\text{g L}^{-1}$ ,  $30 \mu\text{g L}^{-1}$ , and  $6 \mu\text{g L}^{-1}$ , respectively.

At this point, it is important to highlight that pH 4 was chosen to perform these experiments, since hydroxyl radicals are predominantly formed in neutral or basic pH, whereas the stability of ozone molecules are higher in acidic pH, and is thus more difficult to decompose [33]. Thus, in acidic pH, the catalysts have a much more important role in the radicals' formation than in other pHs. Moreover, the phosphate buffer was chosen, since phosphate radicals may act as secondary chain promoters and may also significantly increase ozone destruction at low pH 4, being more pronounced at higher ionic strength [34].



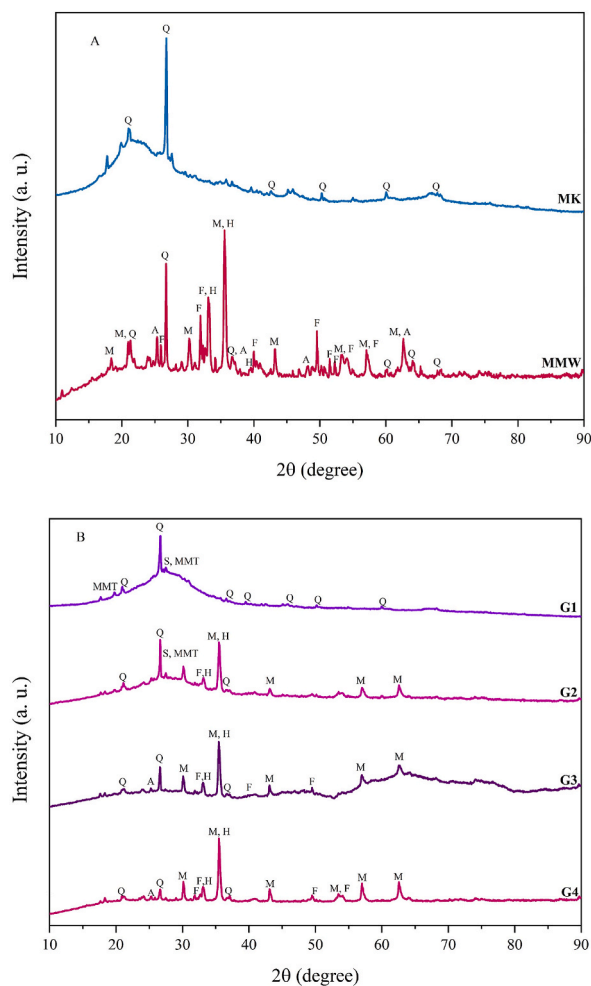


**Fig. 1.** XRD patterns of the precursors materials (A) and the different geopolymer compositions (B) (Q – quartz, M – magnetite, H – hematite; F – fluorapatite, A – anatase, S – sanidine, MMT – montmorillonite).

mining residue, very commonly found in Catalão (Goiás), Brazil [26].

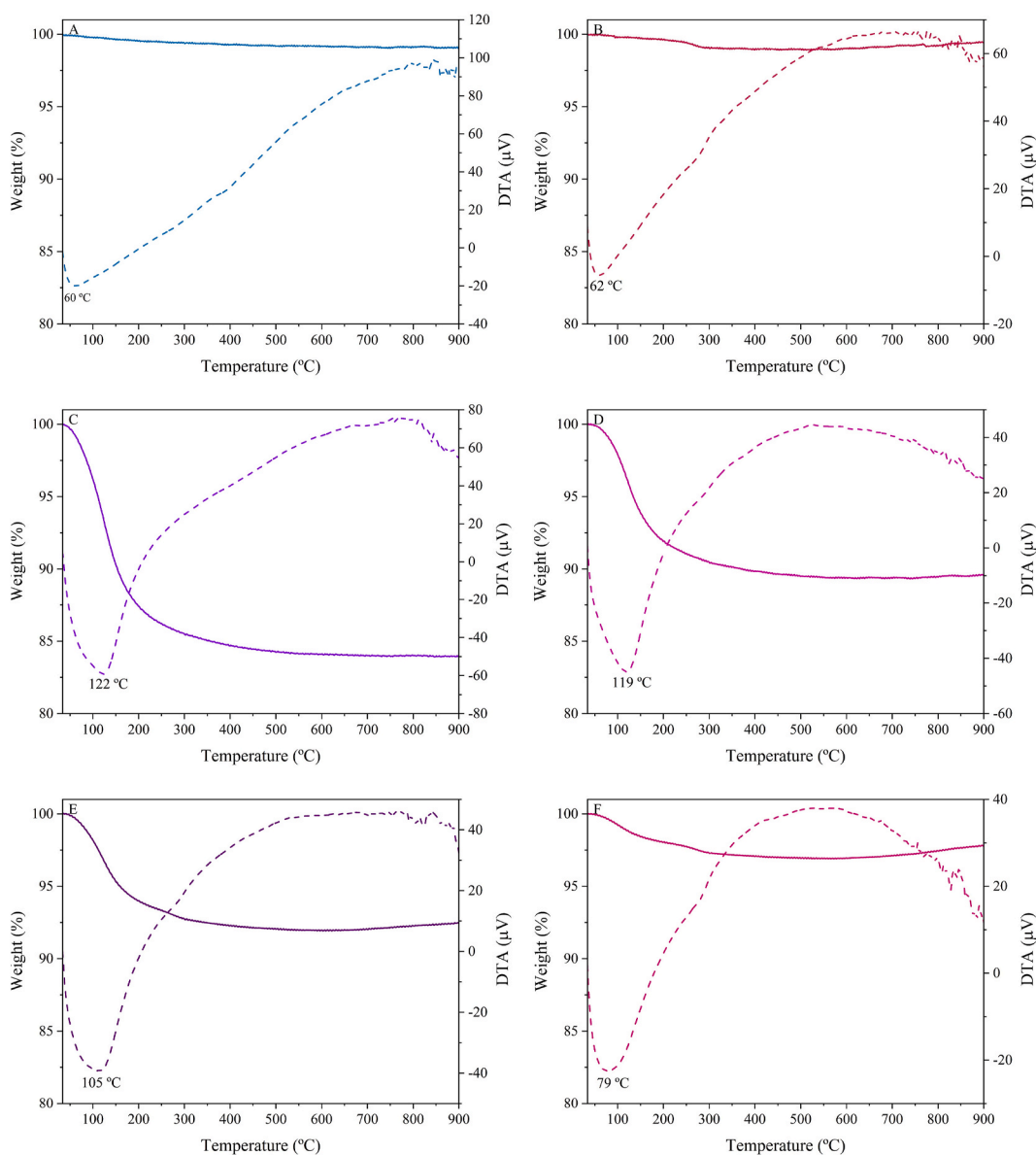
G1 was composed of quartz ( $\text{SiO}_2$  – JCPDS 46–1045) and two different aluminosilicates: montmorillonite ( $\text{Na}_x(\text{Al}, \text{Mg})_2\text{Si}_4\text{O}_{10}(\text{OH})_2 \cdot z\text{H}_2\text{O}$  – JCPDS 12–0204) and sanidine ( $(\text{Na}, \text{K})(\text{Si}_3\text{Al})\text{O}_8$  – JCPDS 10–0357) (Fig. 1B), and the emergence of these new crystalline phases demonstrate the formation of new Si/Al-based polymers. In addition, aside from the previously identified phases, sample G2 also presented peaks corresponding to magnetite ( $\text{Fe}_3\text{O}_4$  – JCPDS 75–1609), hematite ( $\alpha\text{-Fe}_2\text{O}_3$ , – JCPDS 01-085-0987), fluorapatite ( $\text{Ca}_5(\text{PO}_4)_3\text{F}$  – JCPDS15-0876) and anatase ( $\text{TiO}_2$  – JCPDS 21–1272) in the crystallographic patterns. The appearance of these structures is descendant from the MMW composition, not demonstrating significant incorporation of them into the geopolymeric matrix, since they remained unchanged. It should also be noted that the geopolymers G1 and G2 presented an amorphous hump similar to that observed for the raw MK, while the G3 and G4 samples not only had a composition resembling MMW (i.e., quartz, magnetite, hematite, fluorapatite and anatase) but also had enhanced crystallinity with higher and sharper peaks. Peaks associated with aluminosilicate polymers (such as sanidine and montmorillonite) were not identified in the G3 and G4 samples, probably due to high amounts of incorporated MMW (50–75%), since their geopolymerization could be proven by other techniques as will be discussed next.

The FTIR spectra (Figures S1-S2, Table 3) for the samples presented a superficial O–H stretching band ( $\approx 3486\text{ cm}^{-1}$ ) and H–O–H bending vibrations ( $\approx 1619\text{ cm}^{-1}$ ), associated with adsorbed water [38]. Moreover, MMW also presented an additional O–H stretching peak at  $3062\text{ cm}^{-1}$ , which ascribes to Fe(III) a hydroxide bond present in this residue [39]. All materials presented bands related to Si–O–T asymmetric stretching (where, T = tetrahedral Si or Al) bonds ( $\approx 1031\text{ cm}^{-1}$ ), associated with the aluminosilicate bonds present in these materials [40]. Moreover, the Si–O–T asymmetric stretching bonds showed a small displacement compared with the precursors (up to  $94\text{ cm}^{-1}$ ), related to the formation of a new gel phase [41]. This was also evidenced by the formation of similar Si–O–T asymmetric stretching bonds ( $\approx 585\text{ cm}^{-1}$ ) in G1 and G2, indicating that a denser aluminosilicate framework was formed. This last band peak was not observed for the samples G3 and G4, probably due to a much higher intensity of the overlapping Fe–O stretching

**Table 3**

Major bands in the FTIR spectra and their assignments for the as-synthesized geopolymers and their raw materials.

Band position (cm <sup>-1</sup> )						Band assignment
MK	MMW	G1	G2	G3	G4	
3444	3695	3463	3448	3441	3422	O–H stretching vibration
–	3062	–	–	–	–	
1634	1487	1650	1648	1650	1647	H–O–H bending vibration
–	1090	–	–	–	–	Si–O–T (where T = tetrahedral Si or Al) asymmetric stretching
1094	1039	1018	1021	1015	1000	
–	903	–	–	–	–	Si–OH bending vibration, Si–O stretching
–	–	885	881	877	865	Al–O stretching vibration
807	799	–	–	–	–	Si–O–Si bond (quartz) symmetric stretching
–	–	718	718	712	727	Al–O stretching vibration, Al–O–Si symmetrical elongation
–	693	–	–	–	694	Fe–O stretching vibration (magnetite)
–	600	–	–	601	603	
–	–	586	584	–	–	Si–O–T (where T = tetrahedral Si or Al) symmetric stretching
–	569	–	–	576	570	Fe–O stretching vibration (tetrahedral magnetite)
468	462	447	449	445	455	Si–O–Si bond (SiO <sub>4</sub> tetrahedral) bending

**Fig. 2.** TGA and DTA for the MK (A), MMW (B) and geopolymers with different compositions (G1-G4) (C-F).

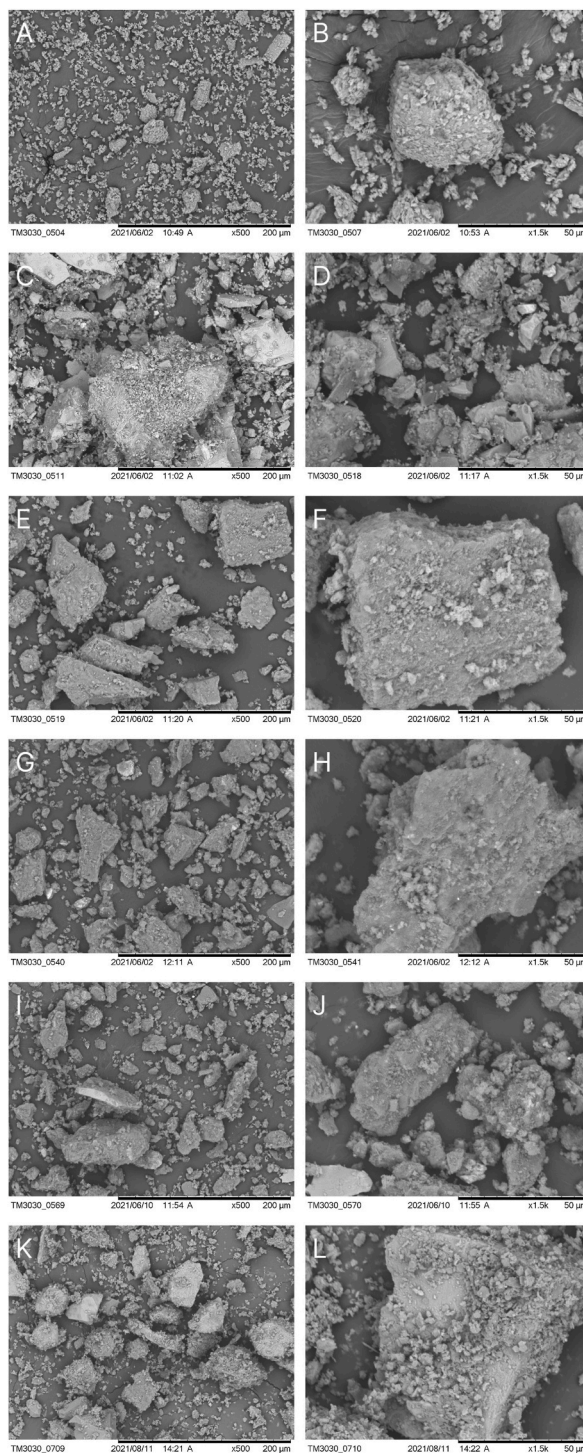


**Fig. 3.** SEM images of MK (A–B), MMW (C–D), and G1–G4 (E–L) powders in two magnifications 500 × (A, C, E, G, I, and K) and 1500 × (B, D, F, H, J, and L).

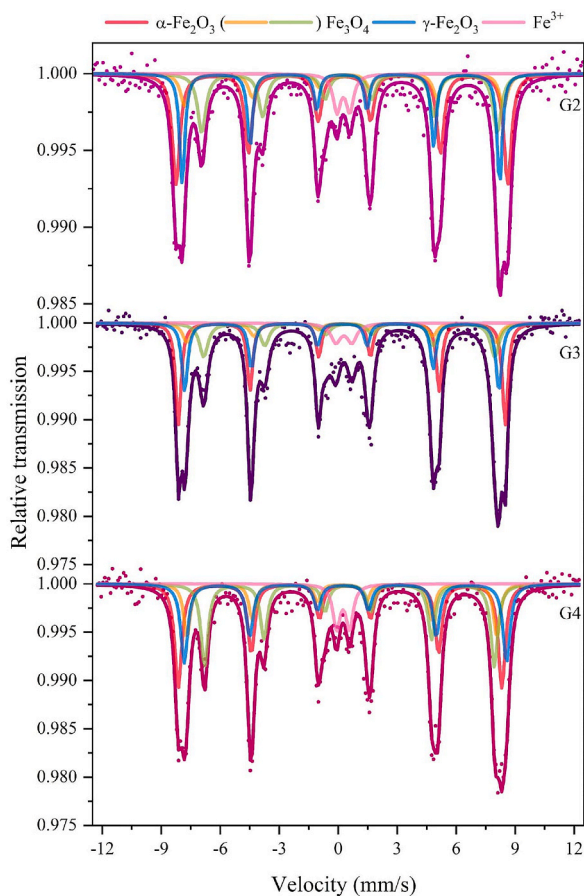
bands of the magnetite ( $\approx 572 \text{ cm}^{-1}$ ) and maghemite ( $\approx 694$  and  $\approx 601 \text{ cm}^{-1}$ ), a defective form of magnetite [42].

Other silicon bonds were also detected: Si–OH bending vibration and Si–O stretching and deformation (at  $903 \text{ cm}^{-1}$  for MMW) [40], along with Si–O–Si symmetric stretching (characteristic of the quartz phase) ( $807 \text{ cm}^{-1}$  for MK and  $799 \text{ cm}^{-1}$  for MMW) and bending (all samples,  $\approx 454 \text{ cm}^{-1}$ ) [11,40,43].

Further evidence of geopolymerization was the appearance of bands ascribed to Al–O stretching vibrations ( $\approx 877$  and  $\approx 719 \text{ cm}^{-1}$ )

**Table 4**  
Surface area, pore volume and average pore size of precursors and as-prepared GPs.

Sample	$S_{\text{BET}}$ ( $\text{m}^2\cdot\text{g}^{-1}$ )	$V_p \times 10^1$ ( $\text{cm}^3\cdot\text{g}^{-1}$ )	Average pore size diameter (nm)
MK	11.3	0.60	21.43
MMW	4.9	0.12	9.32
G1	27.2	2.71	39.91
G2	20.0	1.76	35.13
G3	10.4	1.05	40.26
G4	12.6	0.14	4.58



**Figs. 4.**  $^{57}\text{Fe}$  Mössbauer spectra for the geopolymer materials.

and Al–O–Si symmetrical elongation ( $\approx 719 \text{ cm}^{-1}$ ) [44–46], which cannot be observed in the spectra for the aluminosilicate raw materials.

Lastly, typical bands associated with carbonation (in the regions between  $2600$  and  $2400 \text{ cm}^{-1}$  and  $1500$ – $1400 \text{ cm}^{-1}$ ) were not detected [11,40], with the expectation of the precursor MMW, which has a peak at  $1487 \text{ cm}^{-1}$ , related to the vibration mode of carbonate ions [47] from the mineralogical composition of the earth explored in the mining process.

The thermal behaviors of the precursors and G1–G4 are reported in Fig. 2. Both MK and MMW showed low weight loss (0.92% and 0.56%, respectively). Only one endothermic peak was observed in the DTA thermograms, which corresponds to free water loss, at  $60 \text{ }^\circ\text{C}$  for MK and at  $62 \text{ }^\circ\text{C}$  for MMW [48]. Small weight losses related to dehydration and structural water losses were also observed.

The results obtained for the GPs in the TGA analysis showed a strong relation with the amount of MMW used in their synthesis. The total weight losses from G1 to G4 were 16%, 10%, 8% and 2%, in that order. The greatest mass loss occurred up to  $\approx 150 \text{ }^\circ\text{C}$ , due to the free water loss (representing at least half of the total weight loss) [48], represented by a DTA endothermic peak. As the amount of MMW used in the synthesis increased, the temperature peak decreased from  $122 \text{ }^\circ\text{C}$  to  $79 \text{ }^\circ\text{C}$ , which indicates a weaker hydrophilic bond when compared to GPs with more MK. From  $150 \text{ }^\circ\text{C}$  to  $300 \text{ }^\circ\text{C}$ , a considerable mass loss is still noted (approximately one third of the total mass loss), which could be related to the desorption of water from the geopolymer surface [40]. Since a small decrease occurs between  $300 \text{ }^\circ\text{C}$  and  $600 \text{ }^\circ\text{C}$  (1.4% or less), it is feasible to assume that a small percentage of structural water was lost, because of the

**Table 5**  
Mössbauer hyperfine parameters for the geopolymer materials.

Sample	Site	$\delta$ ( $\pm 0.05$ ) (mm·s <sup>-1</sup> )	$\epsilon$ ( $\pm 0.05$ ) (mm·s <sup>-1</sup> )	$B_{\text{HIF}}$ ( $\pm 0.5$ ) (T)	Relative area ( $\pm 1$ ) (%)
G2	$\alpha$ -Fe <sub>2</sub> O <sub>3</sub>	0.34	-0.12	51.4	38
	Fe <sub>3</sub> O <sub>4</sub>	0.63	0.06	45.8	25
		0.30	-0.02	49.5	14
		0.26	-0.04	49.3	17
	Fe <sup>3+</sup>	0.33	0.71	-	6
G3	$\alpha$ -Fe <sub>2</sub> O <sub>3</sub>	0.35	-0.14	51.6	30
	Fe <sub>3</sub> O <sub>4</sub>	0.65	0.01	45.9	25
		0.31	-0.09	49.0	14
		0.29	-0.04	49.4	23
	Fe <sup>3+</sup>	0.38	0.71	-	9
G4	$\alpha$ -Fe <sub>2</sub> O <sub>3</sub>	0.31	-0.24	51.0	31
	Fe <sub>3</sub> O <sub>4</sub>	0.62	0.07	45.7	25
		0.29	-0.01	48.9	14
		0.32	-0.02	50.1	24
	Fe <sup>3+</sup>	0.34	0.65	-	6

**Table 6**  
Fitting component peaks and their parameters from the deconvolution of the XPS spectra.

Sample	Element [Denotation; E <sub>b</sub> (eV), FWHM (eV); area (%)]	
	Fe 2p	O 1s
G1	-	O1/532.8/1.76/20
	-	O2/531.6/1.89/75
	-	O3/530.4/1.89/5
G2	F1 (Fe <sup>2+</sup> )/724.3/2.79/21	O1/532.8/1.69/18
	F2 (Fe <sup>3+</sup> )/721.5/2.52/8	O2/531.6/1.88/79
	F3 (Fe <sup>2+</sup> )/717.8/3.33/16	O3/529.9/1.53/3
	F4 (Fe <sup>3+</sup> )/713.8/2.52/15	-
	F5 (Fe <sup>2+</sup> )/710.3/3.06/39	-
G3	F1 (Fe <sup>2+</sup> )/725.5/3.22/14	O1/532.9/1.64/12
	F2 (Fe <sup>3+</sup> )/722.5/2.95/14.	O2/531.6/1.37/86
	F3 (Fe <sup>2+</sup> )/718.1/3.76/15	O3/529.6/1.96/2
	F4 (Fe <sup>3+</sup> )/713.6/3.22/22	-
	F5 (Fe <sup>2+</sup> )/710.3/3.49/35	-
G4	F1 (Fe <sup>2+</sup> )/725.4/3.22/19	O1/532.8/1.62/13
	F2 (Fe <sup>3+</sup> )/721.8/2.95/13	O2/531.4/1.94/86
	F3 (Fe <sup>2+</sup> )/717.7/3.76/11	O3/529.4/1.62/1
	F4 (Fe <sup>3+</sup> )/713.5/3.22/18	-
	F5 (Fe <sup>2+</sup> )/710.4/3.49/39	-

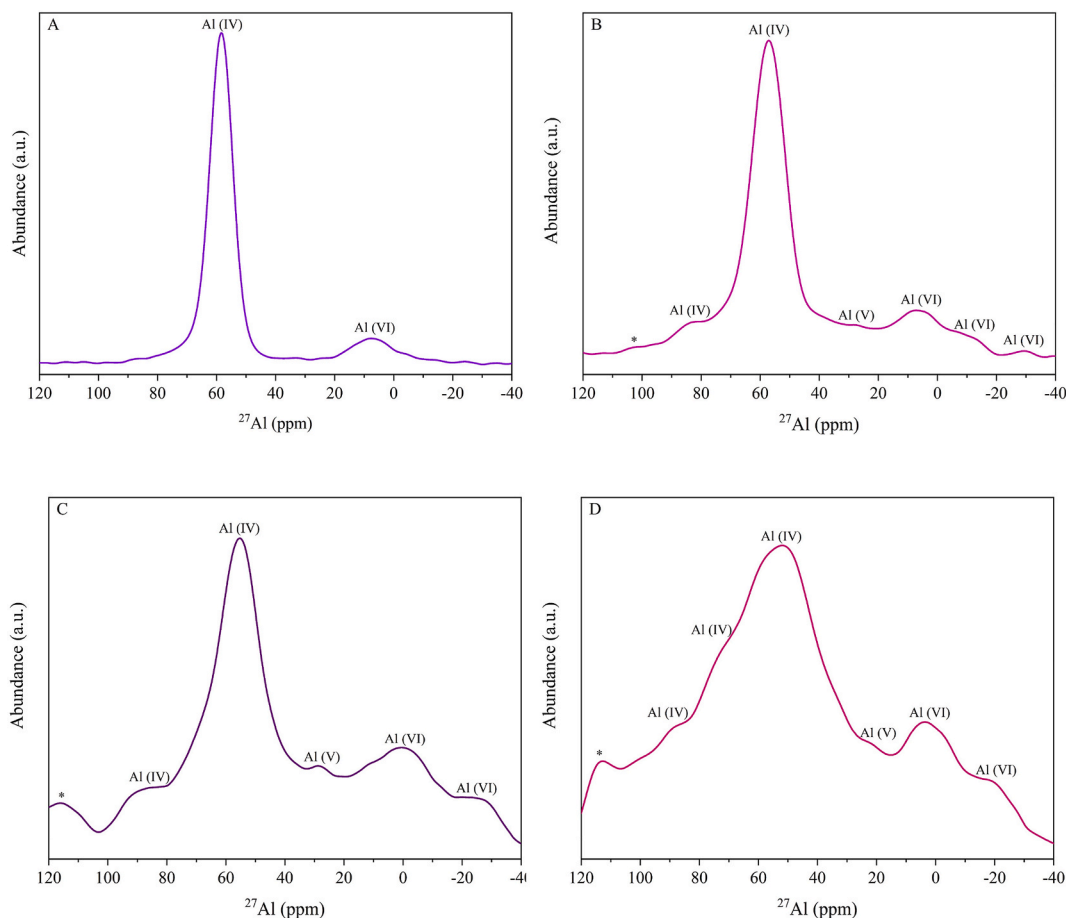
dehydroxylation of the geopolymer frameworks [40]. Moreover, in the range 600 °C - 900 °C, the mass loss was negligible (<0.2%), which indicates that no or insignificant carbonation reactions occur [40]. These small amounts of CO<sub>2</sub> loss can be attributed to low CaCO<sub>3</sub> concentrations in the GP compositions (due to the composition of the raw materials or CO<sub>2</sub> adsorption and subsequent carbonation). These results are in agreement with the previously discussed FTIR results, which demonstrates that the as-synthesized GPs have high resistance to CO<sub>2</sub> contamination [49].

The morphology of the material particles can be seen in Fig. 3. MK appears as agglomerated semi-spherical particles (~8 μm), although asymmetric structures are also observed. However, MMW is constituted by non-uniform polygonal-like particles, similar to previously reported quartz crystals [50], and there is a wide range of particle sizes (0.5–170 μm).

The G1 - G4 particles are similar in shape and size (18 μm, 14 μm, 13 μm and 14 μm, for G1, G2, G3 and G4, respectively) (Fig. 3), appearing as irregular polygonal-like structures, some with sharp edges, due to the cracking and milling processes. In the EDS analysis (Table S3), O, Si, Al (except for sample G4) and Na were detected in all samples. In addition, MMW, G3 and G4 also presented Mg, Ti, Ca, Mn and Fe.

The surface area ( $S_{\text{BET}}$ ), pore volume ( $V_p$ ) and average pore size of the geopolymers are significantly higher than the values of the precursors (Table 4). However, there is no clear relationship between MMW content and surface area. In addition, the  $V_p$  and average pore size values increased for all GPs (except for G4), providing further evidence that new structures and frameworks were formed during the geopolymerization process. The BET surface areas are in the same order of magnitude than other magnetic geopolymers produced by incorporating pure magnetite and a porogenic agent (hydrogen peroxide and soybean oil) in the geopolymer synthesis [38], and 10–24 times higher than others intercalated with Fe<sub>3</sub>O<sub>4</sub> nanoparticles-geopolymeric materials [51].

In addition, all the BET isotherms (Figure S3) were type II with discrete H3-hysteresis [52], typical of plate-shaped particles. This type of curve is typical of physisorption on nonporous or microporous materials, which is a result of monolayer-multilayer adsorption interactions [52]. Moreover, the less distinctive inflection point in G1-G3 samples is an indication of a significant overlap of monolayer



**Figs. 5.**  $^{27}\text{Al}$  solid-state NMR spectra for G1 (A), G2 (B), G3 (C) and G4 (D) (\* corresponds to spinning sidebands (SSB)).

coverage and the multilayer formed [52].

Mössbauer spectroscopy was performed to quantitatively analyze the different Fe species present in the as-prepared geopolymers (Fig. 4 and Table 5). All of the isomer shifts ( $\delta$ ) observed correspond to  $\alpha\text{-Fe}$  structures and the data were ascribed as five Zeeman spectra: one doublet corresponding to  $\text{Fe}^{3+}$  species (6–9%) and four sextets, identified as  $\alpha\text{-Fe}_2\text{O}_3$  (30–38%), A site  $\text{Fe}_3\text{O}_4$  (14%), B site  $\text{Fe}_3\text{O}_4$  (25%) and  $\gamma\text{-Fe}_2\text{O}_3$  (17–24%). Thus, the Fe composition of the sample was, in descending order, magnetite > hematite > maghemite >  $\text{Fe}^{3+}$ . Both the  $\text{Fe}_3\text{O}_4$  sextets are related to tetrahedral ( $\delta \cong 0.30 \text{ mm s}^{-1}$ ,  $B_{\text{HF}} \cong 49.1 \text{ T}$ ) and octahedral ( $\delta \cong 0.63 \text{ mm s}^{-1}$ ,  $B_{\text{HF}} \cong 45.8 \text{ T}$ ) environments of magnetite [53]. In addition, these peaks show approximately a 1:2 intensity ratio, typical of stoichiometric magnetite [53]. It can be noted that the geopolymerization process did not significantly modify the MMW composition (Figure S4 and Table S4), which presented equivalent peaks and relative areas.

Moreover, the fact that  $\text{Fe}^{3+}$  relative areas remained similar, combined with the previously reported XRD, as well as the obtained isomer shifts ( $\delta$ ), and quadrupole splitting/quadrupole shift ( $\Delta/\epsilon$ ) parameters, it seems that Fe oxides had little or no incorporation to the geopolymer network [54].

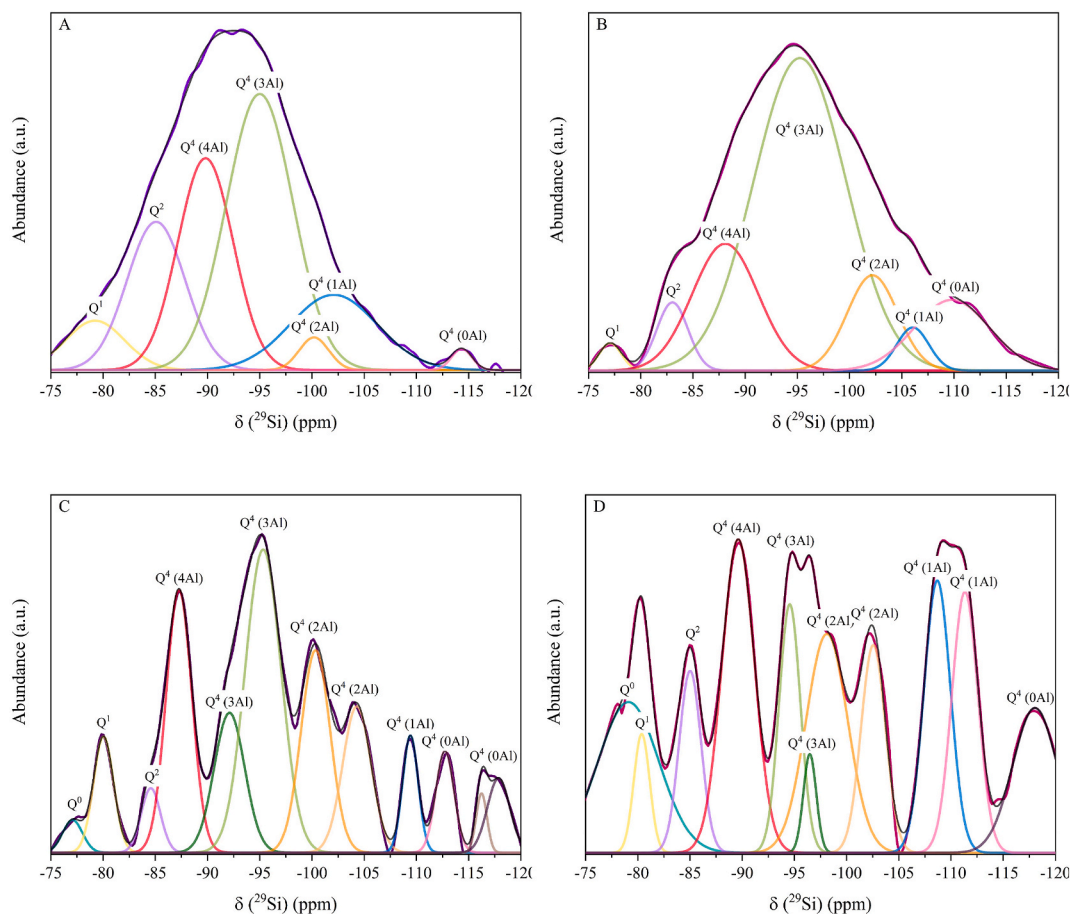
The survey XPS spectra (Figure S5A–D) were studied and the characteristic photoemissions corresponding to Si (2p), Al (2p), Fe (2p), Na (1s) and O (1s) were observed [55–57]. In addition, MMW (Figure S5E) also had Ca (2p) in its composition, which was not observed on the surface of the other samples, probably due to its very low amount. The high resolution XPS spectra of Al 2p, Si 2p, Fe 2p and O 1s are shown in Figures S5–S8 and their deconvolution parameters are summarized in Table 6.

In the region corresponding to the Al 2p, the peaks (Figure S6) appear at  $\sim 74.1 \text{ eV}$  related to the geopolymer network formation Al–O–Si, Al–O–Na and Al–O–H bonds [44,58]. A similar binding energy value was also observed in the case of MMW (Figure S6E), since the waste material also has aluminosilicates in its composition.

The Si 2p peaks (Figure S7) appear at  $\sim 102.7 \text{ eV}$  corresponding to Si–O–T (sialate) and silica. Once again, the Si 2p signal shows a similar binding energy value for MMW, that corresponds to Si–O–H and  $\text{SiO}_2$ -like bonds.

It can be observed by the measured full width at half maximum (FWHM) that wider peaks were seen for the G2 and G3 samples. These broadenings indicate a higher number of chemical bonds, i. e., a denser framework structure is formed.

However the Fe 2p spectra showed the main peaks of Fe  $2p_{1/2}$  and Fe  $2p_{3/2}$ , typical of  $\text{Fe}_3\text{O}_4$  [57,59], the deconvolution (Figure S8 and Table 6) showed the presence of five peaks for each sample. Fe  $2p_{3/2}$  shows the main peak with  $E_B$  located at  $\sim 710.3 \text{ eV}$  with two



**Figs. 6.**  $^{29}\text{Si}$  solid-state NMR spectra for G1 (A), G2 (B), G3 (C) and G4 (D).

satellites at  $\sim 713.6$  eV,  $\sim 717.8$  eV typical of the presence of  $\text{Fe}^{2+}$  and  $\text{Fe}^{3+}$  [59,60]. In comparison with the MMW precursor (Figure S8E), chemical shifts up to 1.9 eV could be observed, especially for F1 and F2 peaks. This is related to different Fe bonds formed with oxygen or even with the geopolymer matrix [60,61].

Lastly, on the O 1s core level spectra (Figure S9 and Table 6) three contributions were identified: Si–O–Si, –OH or  $\text{O}^{2-}$  bonds at  $\sim 532.8$  eV, Si–O–T at  $\sim 531.6$  eV and Si–O–Na at  $\sim 529.8$  eV [44,62]. The binding energies and FWHM had similar values, while relative areas related to geopolymerization grades increased, indicating that even values as high as 75% of MMW did not hinder the formation of the geopolymer chains, and were able to produce bonds similar to those of a more expensive product (i.e., MK). In addition, MMW had three peaks, with the first the most prominent, associated with –OH or  $\text{O}^{2-}$  bonds (532.2 eV), in relation to the Si–O–T (531.2 eV) and Si–O–M peaks (529.2 eV), where M corresponds to other metals present in the residue, as Ca, Fe, Mg, Mn and Ti (Table 2). The change in the proportional intensity of the peaks also verifies that geopolymerization occurred.

It can be seen in the  $^{27}\text{Al}$  NMR spectra (Fig. 5) that the addition of MMW to the samples led to the appearance of new and wider peaks, which become more pronounced as the amount increases. The most intense peak in all samples is located at  $\sim 56$  ppm, due to tetrahedral aluminum sites (Al(IV)), which are also described in the literature as the typical resonance state of  $\text{Q}^4$ , i.e., an atom of Al surrounded by four –OSi bonds [63]. In samples G2 – G4, aside from this one, other Al(IV) peaks were observed. Those at  $\sim 86$  ppm are correlated to  $\text{Al}(\text{OH})_4^-$  present in the geopolymer pores and to  $\text{Q}^0$  resonance ( $\text{AlO}_4$ ) [63]. Also, the G4 sample has a broadening of the main peak, caused by the appearance of a chemical shift corresponding to  $\text{Q}^2$  aluminosilicate bonds ( $\sim 72$  ppm) [63,64]. Moreover, for G1 and the other samples, another chemical shift (from 20 ppm to  $-20$  ppm) was identified, associated with Al in the octahedral coordination (Al(VI)) [63]. With the exception of G1, the other GPs had an additional octahedral peak at  $-26$  ppm, attributed to hexa-coordinated Al (Al(VI)) [63]. Furthermore, G2, G3 and G4 had another chemical shift at  $\sim 26$  ppm, assigned as the pentahedral coordination of Al (Al(V)) associated with residual unreacted MK [65].

A comparison of the  $^{27}\text{Al}$  NMR spectra for the GPs and their precursors (Figure S10A–B) allows concluding that aluminosilicates in different states were formed during the reaction, since various chemical shifts were not observed in the original samples, demonstrating that a distinct geopolymerization mechanism occurred. However, the waste added was still able to provide bonds mainly in the more desired tetrahedral  $\text{Q}^4$  resonant state for geopolymers.

The  $^{29}\text{Si}$  NMR spectra for the GPs were well fitted ( $>0.99$ ) and mainly composed of  $\text{Q}^4$  structures ( $\geq 75\%$ ) (Fig. 6 and Table S5),

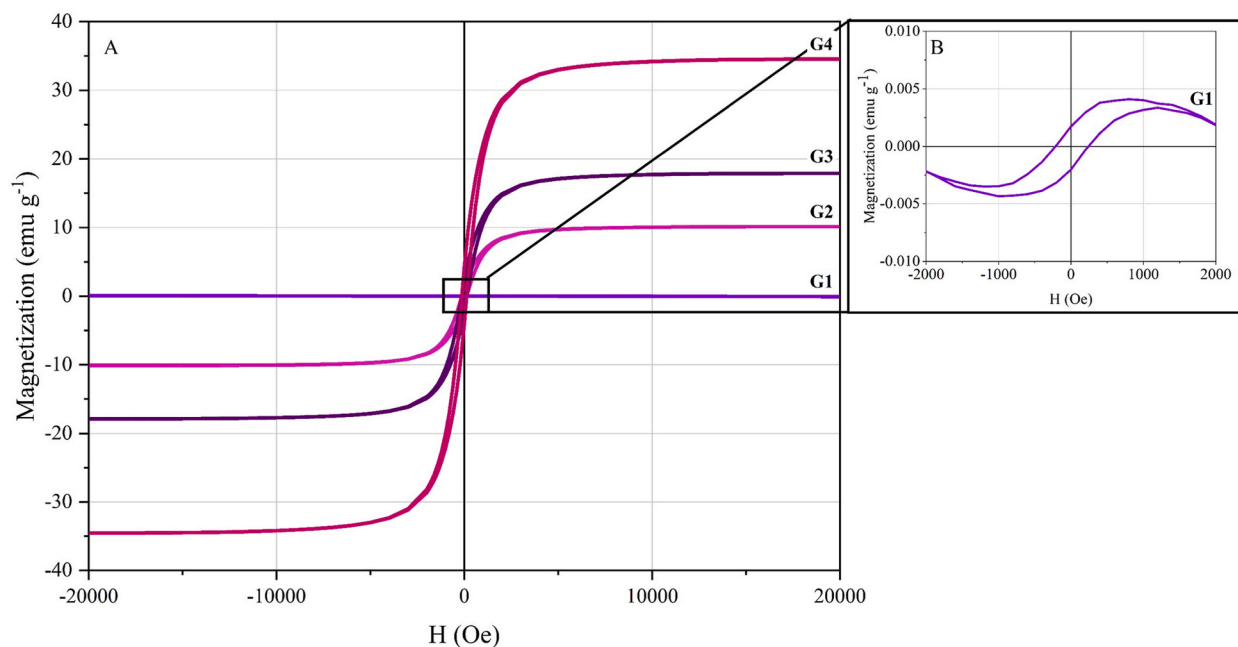


Fig. 7.  $M - H$  curves for the synthesized geopolymers (A) and zoomed in for sample G1 (B).

achieving the highest values of 95% for G2 and 90% for G3. These peaks were centered at  $\sim -89$  ppm,  $\sim -95$  ppm,  $\sim -101$  ppm,  $\sim -106$  ppm and  $\sim -114$  ppm, being related to  $Q^4(4 \text{ A l})$ ,  $Q^4(3 \text{ A l})$ ,  $Q^4(2 \text{ A l})$ ,  $Q^4(1 \text{ A l})$  and  $Q^4(0 \text{ A l})$ , respectively [66,67]. Different types of  $Q^4$  structures are related to the presence of amorphous and crystalline phases [66].

Moreover, less condensed Si species were also observed, that is,  $Q^2$  ( $-84$  ppm),  $Q^1$  ( $-79$  ppm) and  $Q^0$  ( $-78$  ppm), corresponding, in this order, to monomers, dimers and bridging groups [46]. In the case of G1 and G4, these units had high values (23–25%), which is correlated to a high content of an amorphous phase, i.e., lower crystallization.

MK and MMW were mainly composed of short  $Q^4$  structures ( $Q^4(2 \text{ A l})$  and  $Q^4(1 \text{ A l})$ ) (Figure S10C-D), indicating a previous aluminosilicate network. Additionally, the significant changes in the  $^{29}\text{Si}$  NMR spectra indicate that MMW is suitable for alkali activated reactions, leading to the formation of several bonds with dense geopolymerization.

The  $M - H$  curves for the precursor materials (Fig. 7) showed a significant and well-defined magnetization saturation from MMW ( $36 \text{ emu}\cdot\text{g}^{-1}$ ), due to the magnetite and maghemite content, while low values were observed for MK ( $6 \times 10^{-3} \text{ emu}\cdot\text{g}^{-1}$ ). The G1 sample (without MMW) had a slightly lower magnetic saturation than MK ( $4 \times 10^{-3} \text{ emu}\cdot\text{g}^{-1}$ ) and the higher the %MMW added to the samples during the synthesis, the higher the magnetic saturation values (10, 18 and  $34 \text{ emu}\cdot\text{g}^{-1}$ , respectively, for G2, G3 and G4) (Table S6). The low values can be associated to the reduced crystallinity degree of the samples [68]. Furthermore, previous studies indicate that magnetic saturations above  $3 \text{ emu}\cdot\text{g}^{-1}$  are high enough to provide adequate magnetic separation of the solid from aqueous solutions under external magnetic fields [38,69]. Thus, the materials produced have characteristics suitable for efficient magnetic separation.

MMW and all the GPs containing this material showed a typical superparamagnetic curve, whereas for MK and G1 the curves were similar to those of ferromagnetic materials. MMW presented little retentivity and coercivity energy (Table S6), unlike MK and G1, for which these parameters were relatively high. This is strongly related to the sample compositions, since the presence of magnetite in MMW generates a high degree of internal ordering of the particles, while the oxides with an unpaired electron in the MK composition (Si, Al, Fe, Na, Mg and K; described in Table 2) result only in ferromagnetic behavior.

### 3.2. Catalytic decomposition of ozone in aqueous suspension

It is known that ozone can react at the metal oxide surface [70,71], producing free radicals, such as  $\bullet\text{OH}$ ,  $\bullet\text{O}_2\text{H}$  and  $\bullet\text{O}_2^-$ . In this study, the proposed mechanism for the heterogeneous catalytic ozone decomposition (Equations I-VI), consists of the interaction of an  $\text{OH}^-$  ion with the catalyst surface (S), due to electronic interactions ( $\text{OH}\cdot\text{S}$ ). The  $\text{O}_3$  then interacts with and/or adsorbs onto the catalyst surface ( $\bullet\text{O}_3\cdot\text{S}$ ), leading to the formation of oxidizing radicals, such as  $\bullet\text{OH}$ . Other less reactive species ( $\bullet\text{O}\cdot\text{S}$ ,  $\bullet\text{OH}_2^-$ ,  $\bullet\text{O}_2^-$ ) may also be formed during the process (Equations III-VIII).

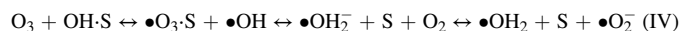
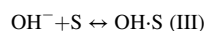


**Table 7**  
Heterogeneous catalytic ozone decomposition constants<sup>a</sup> after 30 min of reaction.

Sample	Ozone decomposition parameters							
	pH	Catalyst dosage (mg·L <sup>-1</sup> )	k <sub>d</sub> (min <sup>-1</sup> )	k <sub>t,a</sub> (min <sup>-1</sup> )	C <sub>e</sub> (mg·L <sup>-1</sup> )	k <sub>het</sub> (L·g <sup>-1</sup> ·min <sup>-1</sup> )	R <sup>2</sup>	Reference
O <sub>3</sub>	4.0	100	0.03	0.63 ± 0.04	5.81 ± 0.07	–	0.993	This study-
MK					2.05 ± 0.02	0.02 ± 0.04	0.994	
MMW					2.01 ± 0.02	0.19 ± 0.01	0.995	
G1					2.13 ± 0.02	2.46 ± 0.05	0.996	
G2					1.58 ± 0.02	2.67 ± 0.05	0.994	Salla et al. (2020)
G3					1.92 ± 0.02	2.97 ± 0.06	0.994	
G4					2.15 ± 0.03	1.00 ± 0.05	0.992	
α-Al <sub>2</sub> O <sub>3</sub>	4.2	100	0.04	0.21	Not specified	0.12 ± 0.02	0.901	
Mn <sub>2</sub> O <sub>3</sub>	5.5		0.06		5.92 ± 0.06	0.12 ± 0.01	0.986	Scaratti et al. (2020)
CuO	5.5	100	0.06	0.48 ± 0.06	4.31 ± 0.01	1.34 ± 0.01	Not specified	

<sup>a</sup> Media conditions: pH = 4; conductivity = 6.511 μS cm<sup>-1</sup>

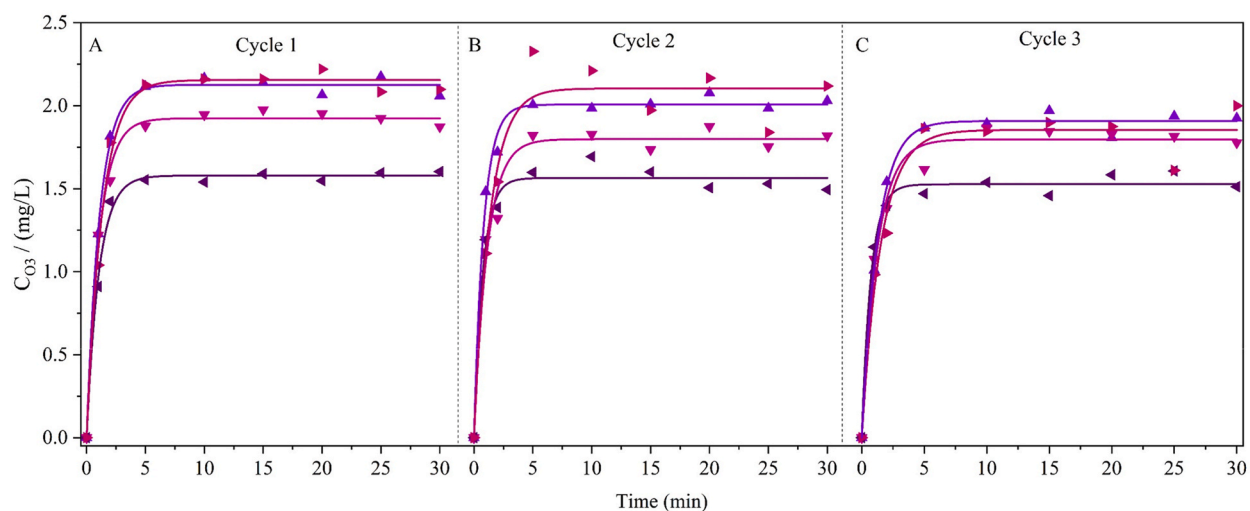
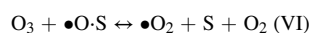


**Fig. 8.** Aqueous ozone concentration over time for three consecutive catalytic ozonation reactions cycles (A–C). Samples are represented as follows: G1 (▲), G2 (▼), G3 (◀), and G4 (◄).



The models were well fitted (Table 7, Fig. 8 and Figure S11) to the proposed mass balance equations (Section I in Supplementary Material) and Table 7 indicates a significant increase in the catalytic ozone decomposition constant ( $k_{\text{het}}$ ) for G1 - G3. G3 was the most active material applied as a catalyst in the ozone decomposition, resulting in the highest  $k_{\text{het}}$  value and the lowest ozone concentration dissolved in the aqueous phase in the stationary state. This indicates a positive synergic effect, due to the combination of aluminosilicates and magnetite in the raw materials, with  $k_{\text{het}}$  being 33 to 99 times greater than the ozone self-decomposition constant ( $k_d$ ).

It is also possible to notice that  $k_{\text{het}}$  values for the geopolymers are much higher than those for MK and MMW. This can be explained by the GPs higher surface area and also their composition (especially G3), which combine various iron oxides (magnetite, maghemite and hematite) with aluminosilicates. This allowed a more efficient ion exchange and/or radicals formation, thus significantly increasing the ozone decomposition rate.

Additionally, the aqueous ozone concentration of equilibrium ( $C_e$ ) was lower for all the applied materials, when compared to water saturation alone (Figure S11), which indicates that ozone interacted with the catalyst surface throughout the reaction, leading to the formation of free radicals. Simultaneous reactions led to the consumption of the remaining O<sub>3</sub> [14], thus reducing the total amount of aqueous ozone available for the saturation of the medium.

Furthermore, these results were compared with previously reported data for other metallic oxides (CuO, Mn<sub>2</sub>O<sub>3</sub> and α-Al<sub>2</sub>O<sub>3</sub>) applied in heterogenous catalytic ozonation under similar conditions (acidic pH, 100 mg L<sup>-1</sup> of catalyst) [71,72]. It can be concluded that the CGPs described herein are promising for this application, since the  $k_{\text{het}}$  values obtained were at least equivalent (G4) and, in some cases, double (G1 – G3) those found in commercial samples.

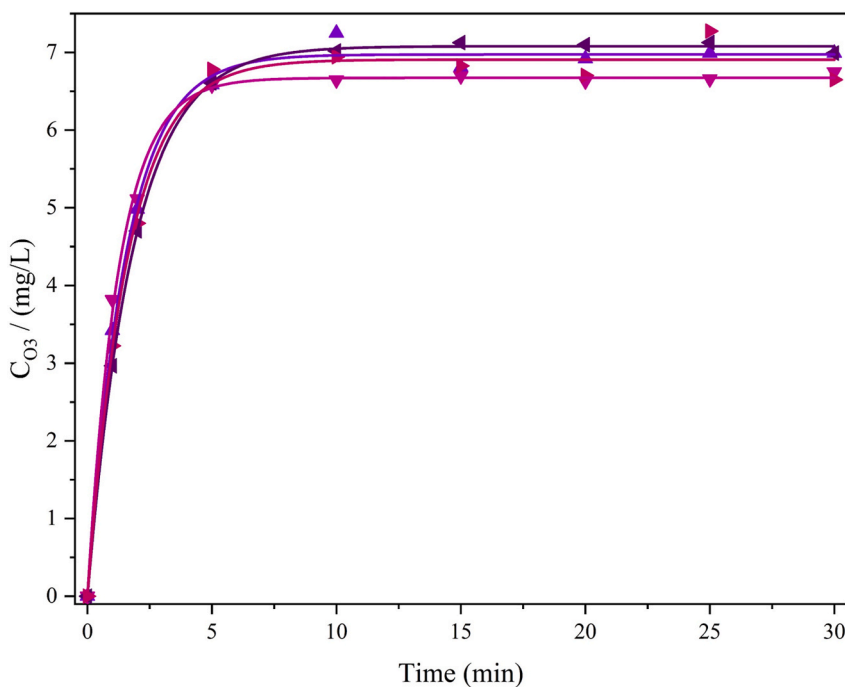


**Fig. 9.** Aqueous ozone concentration over time for the ozonation process for the first cycle solution filtrate. Samples are represented as follows: G1 (—▲—), G2 (—▼—), G3 (—◀—), and G4 (—▶—).

In relation to the recycling studies (Fig. 8), in all three cycles the catalysts maintained similar behavior in the aqueous ozone mass transfer. Again, G3 had better performance, with the lowest ozone saturation value and insignificant variation between the cycles. The other catalysts also had good stability responses, with variations not higher than  $0.3 \text{ mg L}^{-1}$  of aqueous ozone in the solution. Therefore, the reuse of the catalysts combined with their easy removal from the solution by magnetic separation (except from G1) make them quite promising for use in future catalytic reactions.

Finally, hot filtration-like tests were performed by applying the filtrate solution (after the first reaction cycle) to a second ozonation process, without the solids, to prove that the reactions underwent heterogeneous catalysis, and not homogeneous catalysis (descendent from the metals and/or ions leaching from the solids surface). As can be seen in Fig. 9, the aqueous ozone concentration of equilibrium achieved in these investigations were more than three times higher ( $6.67\text{--}6.97 \text{ mg L}^{-1}$ ) than those in experiments in the presence of the solids ( $1.58\text{--}2.15 \text{ mg L}^{-1}$ ) (Fig. 8), achieving values close to that observed for ozonation alone ( $5.81 \text{ mg L}^{-1}$ ). The higher concentration obtained for the hot filtration reactions can be explained by the detrition of the buffer, which initiated with a  $3.7 \pm 0.1 \text{ pH}$ , but decreased up to  $3.4 \pm 0.2$  at the end of the second ozonation. Thus, as ozone solubility increases with the pH decay [73], the final aqueous ozone saturation value increased.

Moreover, the AAS results from the filtrate (Table S7) showed that no Al or Fe leaching was detected. Yet, for Si, low concentrations ( $6.6 \text{ mg L}^{-1}$ ) were observed only in the solution from the G1 sample, while for G2-G4 the values were below the minimum quantification limit (MQL) of  $300 \mu\text{g L}^{-1}$ . Thus, these results indicate that not only did the iron oxides protect the catalysts from leaching but that the aluminosilicate source from MMW produced a final geopolymeric matrix with more stability and ozone resistance.

#### 4. Conclusions

Magnetic mining waste (MMW) material originating from a phosphate mine was used as an aluminosilicate source for the production of geopolymers. The MMW exhibits a notable abundance of iron oxides, including hematite, maghemite, and particularly magnetite. The presence of these iron oxides makes the MMW a favorable catalyst material, facilitating convenient magnetic separation from the system.

Through this research, four distinct geopolymer mixtures were successfully produced, incorporating MK and MMW at varying proportions (0–75%). Notably, all samples demonstrated a well-developed geopolymer framework characterized by a high degree of geopolymerization, minimal carbonation, high surface area, and excellent thermal stability.

In particular, the materials produced are suitable for application as catalysts in heterogeneous ozonation reactions, and not only present catalytic activity, but also achieved values comparable to commercial samples. Thus, these materials could reduce the cost of ozonation treatments while also aggregating value to this residue, which is produced on a large scale. The promising results obtained suggest that these GPs could also be used in other catalytic reactions, which should be further explored in future research.

## Author contribution statement

**Daniela Gier Della Rocca:** Conceived and designed the experiments; Performed the experiments; Analyzed and interpreted the data; Wrote the paper.

**Flávio Augusto Santos e Sousa:** Performed the experiments; Analyzed and interpreted the data.

**José Domingos Ardisson, Rosely Aparecida Peralta, and Enrique Rodríguez-Castellón:** Analyzed and interpreted the data; Contributed reagents, materials, analysis tools or data.

**Regina de Fátima Peralta Muniz Moreira:** Conceived and designed the experiments; Analyzed and interpreted the data; Contributed reagents, materials, analysis tools or data; Wrote the paper.

## Data availability statement

Data will be made available on request.

## Declaration of competing interest

The authors declare that they have no known competing financial interests or personal relationships that could have appeared to influence the work reported in this paper.

## Acknowledgements

The authors would like to acknowledge the Coordination for the Improvement of Higher Education Personnel (CAPES - Brazil) (Project Number 88881.142487/2017–01) and Grant code 001; Brazilian Council for Scientific and Technological Development (CNPq - Brazil) [Grant 405.892/2013-6; 142.059/2019-6; 405.223/2018-8] for financial support. We are also grateful to LINDEN (Interdisciplinary Laboratory for the Development of Nanostructures), LabMat (Materials Laboratory), EQA-UFSC Analysis Center, and LabCAM (Multiuser Laboratory for Magnetic Characterization of Materials) for the XRD, SEM, BET, and VSM analyses, respectively. This research was also funded by the Ministry of Science, Innovation and Universities (Spain), Grant Nos. RTI2018-099668-B-C22 and project UMA18-FEDERJA-126 and P20\_00375 of Junta de Andalucía and FEDER funds. The authors would also like to acknowledge professor Juan Manuel Lazaro Martinez and Elena Rodríguez Aguado for their contributions in NMR and XPS analyses, respectively.

## Appendix A. Supplementary data

Supplementary data to this article can be found online at <https://doi.org/10.1016/j.heliyon.2023.e17097>.

## Appendix - supplementary material

The supplementary material for “Catalytic geopolymers synthesized with magnetic mining waste applied to ozonation reactions” can be found in the Appendix ([Supplementary Material](#)).

## Abbreviations

OH	Hydroxyl radical
AA	Atomic absorption spectrophotometry
AOP	Advanced oxidation processes
CGP	Catalytic geopolymers
DTA	Differential thermal analysis
EDS	Energy dispersive spectroscopy
FTIR	Fourier transform infrared spectroscopy
GP	Geopolymer
JCPDS	Joint Committee on Powder Diffraction Standards
MK	Metakaolin
MMW	Magnetic mining waste
MQL	Minimum quantification limits
ss-NMR	solid state-Nuclear magnetic resonance spectroscopy
SEM	Scanning electron microscopy
TGA	Thermogravimetric analysis
XRD	X-ray diffraction
XPS	X-ray photoelectron spectroscopy
XRF	X-ray fluorescence spectroscopy

## References

- [1] Y.J. Zhang, Z.C. Han, P.Y. He, H. Chen, Geopolymer-based catalysts for cost-effective environmental governance: a review based on source control and end-of-pipe treatment, *J. Clean. Prod.* (2020), 121556, <https://doi.org/10.1016/j.jclepro.2020.121556>.
- [2] T.H. Tan, K.H. Mo, T.C. Ling, S.H. Lai, Current development of geopolymer as alternative adsorbent for heavy metal removal, *Environ. Technol. Innov.* 18 (2020), 100684, <https://doi.org/10.1016/j.eti.2020.100684>.
- [3] J. Davidovits, Procédé de fabrication de panneaux agglomérés et panneaux résultant de l'application de ce procédé, French Patent Application FR 72.38746 (FR 2,204,999) and FR 73.35979 (FR 2,246,382), 1972.
- [4] M.I.M. Al-Zeer, K.J.D. Mackenzie, Fly ash-based geopolymers as sustainable bifunctional heterogeneous catalysts and their reactivity in Friedel-Crafts acylation reactions, *Catalysts* 9 (2019), <https://doi.org/10.3390/catal9040372>.
- [5] C. Bai, P. Colombo, Processing, properties and applications of highly porous geopolymers: a review, *Ceram. Int.* 44 (2018) 16103–16118, <https://doi.org/10.1016/j.ceramint.2018.05.219>.
- [6] P. He, M. Wang, S. Fu, D. Jia, S. Yan, J. Yuan, J. Xu, P. Wang, Y. Zhou, Effects of Si/Al ratio on the structure and properties of metakaolin based geopolymer, *Ceram. Int.* 42 (2016) 14416–14422, <https://doi.org/10.1016/j.ceramint.2016.06.033>.
- [7] S.A. Rasaki, Z. Bingxue, R. Guarecuco, T. Thomas, Y. Minghui, Geopolymer for use in heavy metals adsorption, and advanced oxidative processes: a critical review, *J. Clean. Prod.* 213 (2019) 42–58, <https://doi.org/10.1016/j.jclepro.2018.12.145>.
- [8] A.A. Siyal, M.R. Shamsuddin, M.I. Khan, N.E. Rabat, M. Zulfikar, Z. Man, J. Siame, K.A. Azizli, A review on geopolymers as emerging materials for the adsorption of heavy metals and dyes, *J. Environ. Manag.* 224 (2018) 327–339, <https://doi.org/10.1016/j.jenvman.2018.07.046>.
- [9] Y.J. Zhang, Q. Chai, Alkali-activated blast furnace slag-based nanomaterial as a novel catalyst for synthesis of hydrogen fuel, *Fuel* 115 (2014) 84–87, <https://doi.org/10.1016/j.fuel.2013.06.051>.
- [10] Z. Ji, Y. Zhang, X. Qi, Y. Wang, X. Xia, Y. Pei, Low-cost and facile fabrication of recyclable and reusable waste-based geopolymer for visible-light photocatalysis degradation, *J. Clean. Prod.* 310 (2021), 127434, <https://doi.org/10.1016/j.jclepro.2021.127434>.
- [11] M. Maiti, M. Sarkar, S. Maiti, M.A. Malik, S. Xu, Modification of geopolymer with size controlled TiO<sub>2</sub> nanoparticle for enhanced durability and catalytic dye degradation under UV light, *J. Clean. Prod.* 255 (2020), 120183, <https://doi.org/10.1016/j.jclepro.2020.120183>.
- [12] X. Zhang, X. Zhou, T.B. Moghaddam, F. Zhang, F. Otto, Synergistic effects of iron (Fe) and biochar on light-weight geopolymers when used in wastewater treatment applications, *J. Clean. Prod.* 322 (2021), <https://doi.org/10.1016/j.jclepro.2021.129033>.
- [13] P.Y. He, Y.J. Zhang, H. Chen, L.C. Liu, Development of an eco-efficient CaMoO<sub>4</sub>/electroconductive geopolymer composite for recycling silicomanganese slag and degradation of dye wastewater, *J. Clean. Prod.* 208 (2019) 1476–1487, <https://doi.org/10.1016/j.jclepro.2018.10.176>.
- [14] W. Wang, Z. Chen, Y. Zhou, P. Yan, J. Shen, S. Wang, J. Kang, J. Sun, Z. Wang, Y. Tong, Catalytic ozonation with silicate-based microfiltration membrane for the removal of iopamidol in aqueous solution, *Sep. Purif. Technol.* 257 (2021), 117873, <https://doi.org/10.1016/j.seppur.2020.117873>.
- [15] Y.J. Zhang, L.C. Liu, L.L. Ni, B.L. Wang, A facile and low-cost synthesis of granulated blast furnace slag-based cementitious material coupled with Fe<sub>2</sub>O<sub>3</sub> catalyst for treatment of dye wastewater, *Appl. Catal. B Environ.* 138–139 (2013) 9–16, <https://doi.org/10.1016/j.apcatb.2013.02.025>.
- [16] B.C. McLellan, R.P. Williams, J. Lay, A. Van Riessen, G.D. Corder, Costs and carbon emissions for geopolymer pastes in comparison to ordinary portland cement, *J. Clean. Prod.* 19 (2011) 1080–1090, <https://doi.org/10.1016/j.jclepro.2011.02.010>.
- [17] A. Mehta, R. Siddique, An overview of geopolymers derived from industrial by-products, *Construct. Build. Mater.* 127 (2016) 183–198, <https://doi.org/10.1016/j.conbuildmat.2016.09.136>.
- [18] D.G. Della Rocca, R.M. Peralta, R.A. Peralta, E. Rodríguez-Castellón, R. de Fatima Peralta Muniz Moreira, Adding value to aluminosilicate solid wastes to produce adsorbents, catalysts and filtration membranes for water and wastewater treatment, *J. Mater. Sci.* 56 (2021) 1039–1063, <https://doi.org/10.1007/s10853-020-05276-0>.
- [19] W. Haynes, D. Lide, T. Bruno, *CRC Handbook of Chemistry and Physics*, 2016.
- [20] S.P. Ghuge, A.K. Saroha, Catalytic ozonation for the treatment of synthetic and industrial effluents - application of mesoporous materials: a review, *J. Environ. Manag.* 211 (2018) 83–102, <https://doi.org/10.1016/j.jenvman.2018.01.052>.
- [21] J. Hoigné, *Handbook of Ozone Technology and Application*, Arbor Science Publishers, 1982.
- [22] I. Alaton, I.A. Balcioglu, D. Bahnemann, Advanced oxidation of a reactive dye bath effluent: comparison of O<sub>3</sub>, H<sub>2</sub>O<sub>2</sub>/UV-C and TiO<sub>2</sub>/UV-A processes, *Water Res.* 36 (2002) 1143–1154, <http://www.ncbi.nlm.nih.gov/pubmed/11902771>.
- [23] Y. Ruan, L. Kong, Y. Zhong, Z. Diao, K. Shih, L. Hou, S. Wang, D. Chen, Review on the synthesis and activity of iron-based catalyst in catalytic oxidation of refractory organic pollutants in wastewater, *J. Clean. Prod.* 321 (2021), 128924, <https://doi.org/10.1016/j.jclepro.2021.128924>.
- [24] J. Wang, Z. Bai, Fe-based catalysts for heterogeneous catalytic ozonation of emerging contaminants in water and wastewater, *Chem. Eng. J.* 312 (2017) 79–98, <https://doi.org/10.1016/j.cej.2016.11.118>.
- [25] L. Su, X. Chen, H. Wang, Y. Wang, Z. Lu, Oxygen vacancies promoted heterogeneous catalytic ozonation of atrazine by defective 4A zeolite, *J. Clean. Prod.* 336 (2022), 130376, <https://doi.org/10.1016/j.jclepro.2022.130376>.
- [26] C.E.D. da Mata, C.A. Pereira, A.C. Silva, P.L.R. de Sousa, Characterization of the Angico dos Dias alkaline-carbonatite complex for phosphate rock processing, *J. Mater. Res. Technol.* 9 (2020) 12236–12243, <https://doi.org/10.1016/j.jmrt.2020.08.094>.
- [27] F. Brandão, F. Gabriel, S. Araújo, Characterization of Magnetic Tailings from Phosphate-Ore Processing in Alto Paranaíba, 2022.
- [28] J. Davidovits, M. Davidovits, N. Davidovits, Process for obtaining a geopolymer-alumino-silicate and products thus obtained 595 (1994).
- [29] A.L. Freire, C.D. Moura-Nickel, G. Scaratti, A. De Rossi, M.H. Araújo, A. De Noni Júnior, A.E. Rodrigues, E.R. Castellón, R. de Fátima Peralta Muniz Moreira, Geopolymers produced with fly ash and rice husk ash applied to CO<sub>2</sub> capture, *J. Clean. Prod.* 273 (2020), <https://doi.org/10.1016/j.jclepro.2020.122917>.
- [30] *Standard Methods, International Standard of the Inhibitory Effect of Water Samples*, 2007, p. 2007.
- [31] R.A. Brand, Improving the validity of hyperfine field distributions from magnetic alloys. Part I: unpolarized source, *Nucl. Instrum. Methods Phys. Res. B* 28 (1987) 398–416, [https://doi.org/10.1016/0168-583X\(87\)90182-0](https://doi.org/10.1016/0168-583X(87)90182-0).
- [32] Jian He, *phdSynthesis and Characterization of Geopolymers for Infrastructural Applications*, Louisiana State University LSU Digital Commons, 2012.
- [33] S. Psaltou, M. Mitrakas, A. Zouboulis, Heterogeneous catalytic ozonation: solution pH and initial concentration of pollutants as two important factors for the removal of micropollutants from water, *Separations* 9 (2022), <https://doi.org/10.3390/separations9120413>.
- [34] L. Fijolek, J. Nawrocki, Phosphate helps to recover from scavenging effect of chloride in self-enhanced ozonation, *Chemosphere* 212 (2018) 802–810, <https://doi.org/10.1016/j.chemosphere.2018.08.148>.
- [35] V.D. Cao, S. Pilehvar, C. Salas-Bringas, A.M. Szczołotok, N.B.D. Do, H.T. Le, M. Carmona, J.F. Rodriguez, A.L. Kjøniksen, Influence of microcapsule size and shell polarity on the time-dependent viscosity of geopolymer paste, *Ind. Eng. Chem. Res.* 57 (2018) 9457–9464, <https://doi.org/10.1021/acs.iecr.8b01961>.
- [36] A.M. Mustafa Al Bakri, H. Kamarudin, M. Bnhussain, I. Khairul Nizar, A.R. Rafiza, A.M. Izzat, Chemical reactions in the geopolymerisation process using fly ash-based geopolymer: a review, *Aust. J. Basic Appl. Sci.* 5 (2011) 1199–1203.
- [37] C.K. Lau, M.R. Rowles, G.N. Parnham, T. Htut, T.S. Ng, Investigation of geopolymers containing fly ash and ground-granulated blast-furnace slag blended by amorphous ratios, *Construct. Build. Mater.* 222 (2019) 731–737, <https://doi.org/10.1016/j.conbuildmat.2019.06.198>.
- [38] D.L. Rossatto, M.S. Netto, S.L. Jahn, E.S. Mallmann, G.L. Dotto, E.L. Foletto, Highly efficient adsorption performance of a novel magnetic geopolymer/Fe<sub>3</sub>O<sub>4</sub> composite towards removal of aqueous acid green 16 dye, *J. Environ. Chem. Eng.* 8 (2020), 103804, <https://doi.org/10.1016/j.jece.2020.103804>.
- [39] P.S. Pinto, G.D. Lanza, J.D. Ardisson, R.M. Lago, Controlled dehydration of Fe(OH)<sub>3</sub> to Fe<sub>2</sub>O<sub>3</sub>: developing mesopores with complexing iron species for the adsorption of β-lactam antibiotics, *J. Braz. Chem. Soc.* 30 (2019) 310–317, <https://doi.org/10.21577/0103-5053.20180179>.
- [40] J.L.V. Lynch, H. Baykara, M. Cornejo, G. Soriano, N.A. Ulloa, Preparation, characterization, and determination of mechanical and thermal stability of natural zeolite-based foamed geopolymers, *Construct. Build. Mater.* 172 (2018) 448–456, <https://doi.org/10.1016/j.conbuildmat.2018.03.253>.

- [41] N. Zhang, A. Hedayat, H.G. Bolaños Sosa, R.P. Huamani Bernal, N. Tupa, I. Yanqui Morales, R.S. Canahua Loza, On the incorporation of class F fly-ash to enhance the geopolymerization effects and splitting tensile strength of the gold mine tailings-based geopolymer, *Construct. Build. Mater.* 308 (2021), <https://doi.org/10.1016/j.conbuildmat.2021.125112>.
- [42] H. Namduri, S. Nasrazadani, Quantitative analysis of iron oxides using Fourier transform infrared spectrophotometry 50 (2008) 2493–2497, <https://doi.org/10.1016/j.corsci.2008.06.034>.
- [43] S. You, S. Wah, T. Li, T. Maneerung, C. Wang, Techno-economic analysis of geopolymer production from the coal fly ash with high iron oxide and calcium oxide contents, *J. Hazard Mater.* 361 (2019) 237–244, <https://doi.org/10.1016/j.jhazmat.2018.08.089>.
- [44] X. Liu, Y. Wu, M. Li, J. Jiang, L. Guo, W. Wang, W. Zhang, Z. Zhang, P. Duan, Effects of graphene oxide on microstructure and mechanical properties of graphene oxide-geopolymer composites, *Construct. Build. Mater.* 247 (2020), 118544, <https://doi.org/10.1016/j.conbuildmat.2020.118544>.
- [45] C. min Li, Y. He, Q. Tang, K. tuo Wang, X. min Cui, Study of the preparation of CdS on the surface of geopolymer spheres and photocatalyst performance, *Mater. Chem. Phys.* 178 (2016) 204–210, <https://doi.org/10.1016/j.matchemphys.2016.05.013>.
- [46] Z. Ji, Y. Pei, Immobilization efficiency and mechanism of metal cations ( $\text{Cd}^{2+}$ ,  $\text{Pb}^{2+}$  and  $\text{Zn}^{2+}$ ) and anions ( $\text{AsO}_4^{3-}$  and  $\text{Cr}_2\text{O}_7^{2-}$ ) in wastes-based geopolymer, *J. Hazard Mater.* 384 (2020), 121290, <https://doi.org/10.1016/j.jhazmat.2019.121290>.
- [47] I. Pálkó, P. Sipos, O. Berkesi, G. Varga, Distinguishing anionic species that are intercalated in layered double hydroxides from those bound to their surface: a comparative ir study, *J. Phys. Chem. C* 126 (2022) 15254–15262, <https://doi.org/10.1021/acs.jpcc.2c03547>.
- [48] H. Cheng, J. Yang, Q. Liu, J. He, R.L. Frost, Thermogravimetric analysis-mass spectrometry (TG-MS) of selected Chinese kaolinites, *Thermochim. Acta* 507–508 (2010) 106–114, <https://doi.org/10.1016/j.tca.2010.05.007>.
- [49] Q. Tian, B. Guo, K. Sasaki, Immobilization mechanism of Se oxyanions in geopolymer: effects of alkaline activators and calcined hydrotalcite additive, *J. Hazard Mater.* 387 (2020), 121994, <https://doi.org/10.1016/j.jhazmat.2019.121994>.
- [50] R.A. Ghashoghchi, M.R. Hosseini, A. Ahmadi, Effects of microbial cells and their associated extracellular polymeric substances on the bio-flocculation of kaolin and quartz, *Appl. Clay Sci.* 138 (2017) 81–88, <https://doi.org/10.1016/j.clay.2017.01.002>.
- [51] A. Maleki, Z. Hajizadeh, V. Sharifi, Z. Emdadi, A green, porous and eco-friendly magnetic geopolymer adsorbent for heavy metals removal from aqueous solutions, *J. Clean. Prod.* 215 (2019) 1233–1245, <https://doi.org/10.1016/j.jclepro.2019.01.084>.
- [52] M. Thommes, K. Kaneko, A.V. Neimark, J.P. Olivier, F. Rodriguez-Reinoso, J. Rouquerol, K.S.W. Sing, Physisorption of gases, with special reference to the evaluation of surface area and pore size distribution (IUPAC Technical Report), *Pure Appl. Chem.* 87 (2015) 1051–1069, <https://doi.org/10.1515/pac-2014-1117>.
- [53] J. Winsett, A. Moilanen, K. Paudel, S. Kamali, K. Ding, W. Cribb, D. Seifu, S. Neupane, Quantitative determination of magnetite and maghemite in iron oxide nanoparticles using Mössbauer spectroscopy, *SN Appl. Sci.* 1 (2019) 1–8, <https://doi.org/10.1007/s42452-019-1699-2>.
- [54] J. Davidovits, R. Davidovits, Ferro-sialate geopolymers (-Fe-O-Si-O-Al-O-), *Tech. Pap.* 27 (2020), <https://doi.org/10.13140/RG.2.2.25792.89608/2>.
- [55] Z. Ji, L. Su, Y. Pei, Synthesis and toxic metals (Cd, Pb, and Zn) immobilization properties of drinking water treatment residuals and metakaolin-based geopolymers, *Mater. Chem. Phys.* 242 (2020), 122535, <https://doi.org/10.1016/j.matchemphys.2019.122535>.
- [56] H. Chen, S. Dong, Y. Zhang, P. He, Robust structure regulation of geopolymer as novel efficient amine support to prepare high-efficiency  $\text{CO}_2$  capture solid sorbent, *Chem. Eng. J.* 427 (2022), 131577, <https://doi.org/10.1016/j.cej.2021.131577>.
- [57] M. Kumari, P. Yadav, Y. Jain, H. Laddha, R. Gupta, Preparation of  $\text{Fe}_3\text{O}_4$ -Cys-Cu magnetic nanocatalyst for expedient synthesis of tripodal C3 symmetric chromofluorogenic receptor for sensing of fluoride ion selectively: an experimental and computational slant, *Mater. Chem. Phys.* 288 (2022), 126360, <https://doi.org/10.1016/j.matchemphys.2022.126360>.
- [58] S. Pu, Z. Zhu, W. Song, H. Wang, W. Huo, J. Zhang, A novel acidic phosphoric-based geopolymer binder for lead solidification/stabilization, *J. Hazard Mater.* 415 (2021), 125659, <https://doi.org/10.1016/j.jhazmat.2021.125659>.
- [59] C. Koo, H. Hong, P.W. Im, H. Kim, C. Lee, X. Jin, B. Yan, W. Lee, H.J. Im, S.H. Paek, Y. Piao, Magnetic and near - infrared derived heating characteristics of dimercaptosuccinic acid coated uniform  $\text{Fe}@\text{Fe}_3\text{O}_4$  core - shell nanoparticles, *Nano Converg* (2020), <https://doi.org/10.1186/s40580-020-00229-4>.
- [60] A. Rajan, M. Sharma, N.K. Sahu, Assessing magnetic and inductive thermal properties of various surfactants functionalised -  $\text{Fe}_3\text{O}_4$  nanoparticles for hyperthermia, *Sci. Rep.* (2020) 1–15, <https://doi.org/10.1038/s41598-020-71703-6>.
- [61] M. Izquierdo, X. Querol, J. Davidovits, D. Antenucci, H. Nugteren, C. Fernández-pereira, Coal fly ash-slag-based geopolymers: microstructure and metal leaching, *J. Hazard Mater.* 166 (2009) 561–566, <https://doi.org/10.1016/j.jhazmat.2008.11.063>.
- [62] M. Mudgal, A. Singh, R.K. Chouhan, A. Acharya, A.K. Srivastava, Fly ash red mud geopolymer with improved mechanical strength, *Clean. Eng. Technol.* 4 (2021), 100215, <https://doi.org/10.1016/j.clet.2021.100215>.
- [63] M. Haouas, F. Taulelle, C. Martineau, Recent advances in application of science Al NMR spectroscopy to materials, *Prog. Nucl. Magn. Reson. Spectrosc.* 94–95 (2016) 11–36, <https://doi.org/10.1016/j.pnmrs.2016.01.003>.
- [64] A. Bouchikhi, W. Maherzi, M. Benzerzour, Y. Mamindy-pajany, Manufacturing of low-carbon binders using waste glass and dredged sediments : formulation and performance assessment at laboratory scale, *Sustainability* 13 (2021) 4960.
- [65] S. Candamano, P. Frontera, A. Macario, F. Crea, J.B. Nagy, P.L. Antonucci, Preparation and characterization of active Ni-supported catalyst for syngas production, *Chem. Eng. Res. Des.* 96 (2015) 78–86, <https://doi.org/10.1016/j.cherd.2015.02.011>.
- [66] G. Fang, M. Zhang, Research Multiscale micromechanical analysis of alkali-activated fly ash-slag paste, *Cement Concr. Res.* 135 (2020), 106141, <https://doi.org/10.1016/j.cemconres.2020.106141>.
- [67] P. Duxson, A. Fernández-Jiménez, J.L. Provis, G.C. Lukey, A. Palomo, J.S.J. van Deventer, Geopolymer technology : the current state of the art, *Adv. Geopolymer Sci. Technol.* (2007) 2917–2933, <https://doi.org/10.1007/s10853-006-0637-z>.
- [68] C.H. Chia, S. Zakaria, M. Yusoff, S.C. Goh, C.Y. Haw, S. Ahmadi, N.M. Huang, H.N. Lim, Size and crystallinity-dependent magnetic properties of  $\text{CoFe}_2\text{O}_4$  nanocrystals, *Ceram. Int.* 36 (2010) 605–609, <https://doi.org/10.1016/j.ceramint.2009.10.001>.
- [69] X. Tao, K. Li, H. Yan, H. Yang, A. Li, Simultaneous removal of acid green 25 and mercury ions from aqueous solutions using glutamine modified chitosan magnetic composite microspheres, *Environ. Pollut.* 209 (2016) 21–29, <https://doi.org/10.1016/j.envpol.2015.11.020>.
- [70] F. Beltrán, *Ozone Reaction Kinetics for Water and Wastewater Systems*, 2004.
- [71] G. Scaratti, A. Basso, R. Landers, P.J.J. Alvarez, G.L. Puma, R.F.P.M. Moreira, Treatment of aqueous solutions of 1,4-dioxane by ozonation and catalytic ozonation with copper oxide (CuO), *Environ. Technol.* 41 (2020) 1464–1476, <https://doi.org/10.1080/09593330.2018.1538259>.
- [72] J.S. Salla, N. Padoin, S.M. Amorim, G. Li, R.F.P.M. Moreira, Engineering Humic acids adsorption and decomposition on  $\text{Mn}_2\text{O}_3$  and  $\alpha\text{-Al}_2\text{O}_3$  nanoparticles in aqueous suspensions in the presence of ozone, *J. Environ. Chem. Eng.* 8 (2020), 102780, <https://doi.org/10.1016/j.jece.2018.11.025>.
- [73] G.V. Egorova, V.A. Voblikova, L.V. Sabitova, I.S. Tkachenko, S.N. Tkachenko, V.V. Lunin, Ozone solubility in water, *Moscow Univ. Chem. Bull.* 70 (2015) 207–210, <https://doi.org/10.3103/S0027131415050053>.